Available online at www.sciencedirect.com
ScienceDirect
Applied Catalysis B: Environmental 78 (2008) 38–52
APPLIED CATALYSIS B: ENVIRONMENTAL
www.elsevier.com/locate/apcatb

A comparative study of $Pt/Ba/Al_2O_3$ and $Pt/Fe\text{-}Ba/Al_2O_3$ NSR catalysts: New insights into the interaction of Pt–Ba and the function of Fe

Jin-Yong Luo [a], Ming Meng [a,*], Yu-Qing Zha [a], Ya-Ning Xie [b], Tian-Dou Hu [b], Jing Zhang [b], Tao Liu [b]

[a] *Department of Catalysis Science and Technology, School of Chemical Engineering and Technology, Tianjin University, Tianjin 300072, PR China*
[b] *Institute of High Energy Physics, Chinese Academy of Sciences, Beijing 100049, PR China*

Received 16 February 2007; received in revised form 18 August 2007; accepted 31 August 2007
Available online 5 September 2007

Abstract

The influence of the introduction of Pt and/or Fe on the structures, NO_x storage property and sulfur removal performance of Ba/Al_2O_3 catalyst was studied. The techniques of TG/DTA, XRD, FT-IR, H_2-TPR, EXAFS and DRIFTS were employed for the careful characterization of the catalysts. Two types of Ba species are identified, namely a well-spread monolayer of Ba species and a bulk $BaAl_2O_4$ phase. The addition of Fe inhibits the Ba dispersion by enhancing the bulk $BaAl_2O_4$ formation, thus slightly decreasing the SO_x absorption and greatly suppressing the growth of the bulk $BaSO_4$, and its addition also promotes the NO_x storage by increasing the mobility of the stored NO_x, contributing to the formation of bulk $Ba(NO_3)_2$. The introduction of Pt always re-disperses the bulk $BaAl_2O_4$ phase via a hydration process, and enhances both the NO_x and SO_x absorption capacity of the catalyst. Whereas the co-existence of Pt and Fe was detrimental for the NO_x storage and sulfur removal as compared with $Pt/Ba/Al_2O_3$ catalyst, although it favors the reduction of $BaSO_4$ phase. Based upon the EXAFS, in situ DRIFTS and repeated H_2-TPR results, it is found that the interaction between Pt and Ba species is of great importance for NO_x storage and sulfur removal. This Pt–Ba interaction not only accelerates the NO_x spillover which is a key step during storage, but also facilitates the selective reduction of $BaSO_4$ into H_2S, favorable to sulfur removal and catalyst regeneration. The introduction of Fe to the $Pt/Ba/Al_2O_3$ catalyst decreases this Pt–Ba interaction by encapsulation of Pt in the matrix of Fe/FeO_x lattice after repeated redox cycles, leading to the decrease of NO_x storage capacity (NSC) of the catalyst, and making sulfur removal more difficult since Fe selectively catalyzes the reduction of $BaSO_4$ into BaS.

Keywords: Pt; Fe; NO_x storage; Sulfur removal; Pt–Ba interaction

1. Introduction

The need for high fuel efficiency and less carbon dioxide emission contributes to the extensive application of the lean-burn engines. However, due to the presence of excess oxygen in the emission, the conventional three-way catalyst (TWC) cannot reduce NO_x effectively [1]. Although considerable efforts have been made on the selective catalytic reduction (SCR) of NO_x, and many examples of catalysts in the literature give high NO_x conversion (>80%) in laboratory tests, this technique cannot be applied for practical use in real automobile exhaust catalysis because of the low space velocities, narrow temperature windows and insufficient durability [2].

Within the last decade, a new concept NO_x storage-reduction (NSR) was developed [3,4] and the catalysts were first put into the markets in Japan. The NSR catalysts mainly consist of three components: (1) noble metals, mainly Pt or Pt–Rh alloy for NO_x oxidation and reduction; (2) alkali or alkaline oxides, mainly BaO for NO_x storage as nitrates due to its high NO_x storage capacity and high rate for NO_x uptake; (3) Al_2O_3 support. During the lean conditions, the NO_x is oxidized and stored as nitrates in a barium-based storage medium. When the engine is switched to a reducing atmosphere, the NO_x stored as nitrates is released and reduced to N_2.

Although numerous investigations on the NSR catalysts have been conducted and theoretical models for NO_x storage have been developed [5–13], problems still remain. Despite the

* Corresponding author. Tel.: +86 22 2789 2275; fax: +86 22 2740 5243.
E-mail address: mengm@tju.edu.cn (M. Meng).

0926-3373/$ – see front matter © 2007 Elsevier B.V. All rights reserved.
doi:10.1016/j.apcatb.2007.08.017

continuous efforts to remove sulfur from the fuels, real automobile exhaust still contains a little sulfur in the form of sulfur dioxide (SO_2), which will deactivate the NSR catalysts. The deactivation process could be mainly ascribed to the formation of alkaline earth metal sulfate complexes under lean-burn conditions, which is thermodynamically stable even at high temperature [14,15]. The temperature at which sulfates can be removed from barium-containing traps under reducing conditions is much higher than the optimum temperature at which nitrates are stored under oxidizing conditions. Thus the need for catalytic materials that remain stable and active over long periods in the presence of poisoning compound SO_2, presents a great challenge.

For solving this problem, many methods have been developed [16–21]. Among them, the addition of the transition metal iron to the NSR catalysts seems to be one of the most promising and practical ways to improve the sulfur tolerance. More and more studies are directed to the effect of Fe, but opinions vary from person to person. Yamazaki et al. [20] reported that the Fe-compound can lower the desorption temperature of the sulfate complexes by limiting the size of the barium sulfate particles. Fanson et al. [21] reported that the sites in the iron phase, which are sulfur resistant, could function for NO_x storage. However, Hendershot et al. found that with the addition of Fe, the overall resistance to SO_2 is not significantly improved [22], and the Fe weight loading has a much smaller effect than Pt and Ba weight loading on the performance of NSR catalysts [23]. In another report [24], even a detrimental effect of the iron introduction on the NO_x storage capacity can be observed by comparing the alumina supported catalyst Pt/Ba/Al_2O_3 (26.3 wt%Ba, 1.5 wt%Pt) and catalyst Pt/Fe/Ba/Al_2O_3 (28 wt%Ba, 1.5 wt%Pt, 11 wt%Fe). The latter generally exhibits much lower amounts of stored NO_x than the former at temperatures above 250 °C. The author concluded that the catalyst preparation techniques affect the performance of the catalyst. It is well established that the preparation methods can greatly influence the component interactions, thus proper knowledge of these interactions by careful catalyst characterization, especially after introducing another transition metal oxide, is a necessary prerequisite for optimizing the catalyst formula and preparation, as well as for regeneration of NSR catalysts.

Unfortunately, the conventional characterization techniques cannot provide useful information due to the small amount and high dispersion of the noble metal, which serves as a key component for storage and regeneration. The surface sensitive method XPS also failed to provide precise information about the chemical state of the noble metal, due to the appropinquity of the binding energy between Pt_{4f} and Al_{2p}. In this work, the extended X-ray absorption fine structure (EXAFS) technique was applied for the characterization of the state of Pt in the catalysts under different treatments. The structures of the Pt and Fe promoted Ba/Al_2O_3 catalysts were also systematically investigated by using the techniques of thermal gravimetric analysis and differential thermal analysis (TG-DTA), X-ray powder diffraction (XRD), temperature-programmed reduction by H_2 (H_2-TPR), Fourier transform infrared spectroscopy (FT-IR), and in situ diffuse reflectance infrared spectroscopy (DRIFTS). The component interactions determined by the catalyst structures are elucidated, and their influence on the catalytic performance including NO_x storage and sulfur removal efficiency, is discussed in detail as well.

2. Experimental

2.1. Catalyst preparation

The Pt/(Fe-)Ba/Al_2O_3 catalyst was prepared by using wet impregnation method. At first, γ-Al_2O_3 (300 m^2/g) was impregnated by the solution containing barium nitrate and/or iron nitrate. Because of the low solubility of the barium nitrate salt, this step was performed at 80 °C. After drying at 110 °C for 12 h and calcination at 600 °C for 6 h in air (temperature of bulk $Ba(NO_3)_2$ decomposition: 574 °C), the resultant solid products were denoted as Ba/Al_2O_3 and Fe-Ba/Al_2O_3. These solids were again impregnated by chloroplatinic acid, followed by drying at 110 °C for 3 h and calcination at 600 °C for 1 h in air. The loadings of Pt, Fe and Ba are 1.5, 7.6 and 15% by weight, respectively. The Pt and Ba loadings were selected on the basis of literature [23], where the optimum catalyst with maximum storage and reduction capability contains 1.25–1.5%Pt and 15–25%Ba by weight. For comparison, Ba/Al_2O_3-TS sample was prepared by a two-step wet impregnation (each time 7.5 wt%Ba was supported), and this catalyst was further impregnated with Fe, denoted as Fe/Ba/Al_2O_3-TS.

2.2. Catalyst pretreatments—reduction, oxidation and sulfation

For investigating the changes in the state of Pt under redox conditions, part of the fresh Pt-containing catalysts were reduced under pure hydrogen at 500 °C for an hour, denoted as Pt/(Fe-)Ba/Al_2O_3-R; the reduced catalysts were further oxidized in air at 300 or 500 °C for an hour, denoted as Pt/(Fe-)Ba/Al_2O_3-O-300 or Pt/(Fe-)Ba/Al_2O_3-O-500.

The catalyst sulfation was carried out at 400 °C for 2 h in a gas-flow microreactor (i.d. 8 mm) with the gas mixture containing 500 ppm (vol) SO_2, 5 vol%O_2, and N_2 for balance. The gas hourly space velocity (GHSV) is 240,000 h^{-1}.

2.3. Catalyst characterization

2.3.1. TG/DTA

A Perkin-Elmer Diamond TG/DTA instrument was used to obtain TG/DTA profiles. For clarity, the differential TG curve (DTG) was also presented. Each time, approximate 20 mg of the sample was heated in air flow (100 ml/min) at a heating rate of 10 °C/min.

2.3.2. XRD

X-ray diffraction measurement was carried out on an X'pert Pro rotatory diffractometer operating at 40 mA and 40 kV using Co Kα as radiation source (λ = 0.1790 nm). The data of 2θ from 20° to 90° were collected with a stepsize of 0.033°.

2.3.3. EXAFS

EXAFS measurements were performed on the 1W1B beamline of Beijing Synchrotron Radiation Facility (BSRF) operating at the condition of ~80 mA and ~2.2 GeV. The spectra of the Pt L_{III}-edge of the catalysts under different pretreatments and the reference compounds were recorded at room temperature in fluorescence mode. A Si(1 1 1) double-crystal monochromator was used to reduce the harmonic content of the monochrome beam. EXAFS data have been analyzed by using the WinXAS program. After two-polynomial-fit background correction, conversion into k space and μ_0 fit, the back-subtracted EXAFS function was weighted by k^3 in order to compensate for the diminishing amplitude due to the decay of the photoelectron wave. The Fourier transforming of the k^3-weighted EXAFS data into radial structure function (RSF) was performed in the range $k = 3–14\ A^{-1}$ with a Hanning window function. The coordination peaks in RSF are back-transformed separately and fitted by experimental phases, in order to obtain the structural parameters such as coordination number and distances. The experimental phase shifts and backscattering amplitudes were extracted from the reference compounds: PtO_2 for Pt–O, and Pt foil for Pt–Pt.

2.3.4. TPR

The H_2-TPR measurements were performed on a Thermo-Finnigan TPDRO 1100 instrument with a thermal conductivity detector (TCD). The reducing gas was 5 vol%H_2 balanced by pure N_2, and a flow rate of 20 ml/min was used. The quartz tube reactor was loaded with 50 mg sample in powder form at a rate of 10 °C/min. Before detection by the TCD, the gas was purified by a trap containing CaO + NaOH materials in order to remove the H_2O, H_2S, SO_2 and CO_2. For the repeated TPR cycles, the sample was reduced from RT to 600 °C at a rate of 10 °C/min and hold for 15 min, then the reduced sample was oxidized under 6 vol% O_2/He with a flow rate of 20 ml/min from RT to 600 °C at a rate of 10 °C/min and hold for 1 h to ensure complete oxidation of the sulfides to sulfates [25], and finally the next TPR test was performed. The TCD signal was quantitatively calibrated by monitoring the reduction of known amounts of high-purity CuO (99.9999%, Alfa Aesar).

2.3.5. FT-IR and in situ DRIFTS

The FT-IR and DRIFTS experiments were performed on a Nicolet Nexus spectrometer. For FT-IR studies, a fraction of the sulfated catalyst was diluted into KBr and pressed in the form of a pellet. For the DRIFTS study, the spectrometer was equipped with a MCT detector cooled by liquid nitrogen, and a heating chamber allowed samples to be heated up to 600 °C. The DRIFTS spectra were recorded against a background spectrum of the sample purified just prior to introducing the adsorbates. In each run, about 15 mg of the sample in powder form was used.

The NO_x adsorption was carried out in order to get information on the NO_x storage mechanism. The sample was pretreated in a helium (99.999%) flow of 30 ml/min at 300 °C for 15 min, and then exposed to a flow 400 ppm NO. The spectra of NO adsorption at 300 °C were recorded at a spectral resolution of $4\ cm^{-1}$. The NO adsorption under oxidizing condition was performed by using dry air to replace the helium.

The CO chemisorption was conducted for investigating the chemical state of Pt on the surface. The reduced sample was purified in a helium (99.999%) flow of 80 ml/min at 500 °C for half an hour and cooled down to 25 °C, then exposed to the 4 vol%CO/He flow of 80 ml/min for half an hour to saturated adsorption and flushed with helium flow again. The spectra of CO adsorption at 25 °C were recorded at a spectral resolution of $2\ cm^{-1}$.

2.4. NO_x storage capacity (NSC) measurement

NO_x storage measurement was performed in a continuous fixed-bed quartz tubular reactor (i.d. 8 mm) mounted in a tube furnace at 300 °C under atmosphere pressure. The feed gas (380 ppm NO, 5%O_2 and balance N_2) passed through the catalyst (0.4 g, ca. 0.8 ml) at a space velocity of 30,000 h^{-1}. An on-line EC 9841-AS NO_x analyzer (ECOTECH, chemiluminescence detector) was used to measure the NO_x concentration.

3. Results and discussion

3.1. TG/DTA and XRD during preparation

The TG/DTA profiles of the samples during the preparation are shown Fig. 1. All the peaks below 100 °C on the DTG curves correspond to desorption of physically absorbed water. Fig. 1(a) shows that the thermal decomposition of $Ba(NO_3)_2$ supported on Al_2O_3 is in two steps within the range of 400–700 °C. The temperature for the first step is much lower than that for bulk $Ba(NO_3)_2$ decomposition (574 °C), which should be related to the high dispersion or small crystallites of $Ba(NO_3)_2$ on the Al_2O_3 support, such as the well-spread or a monolayer $Ba(NO_3)_2$ phase. In the second step, the peak zenith temperatures are almost the same as the bulk $Ba(NO_3)_2$, which could be assigned to the decomposition of large crystal $Ba(NO_3)_2$. The DTG profiles for iron nitrate impregnated, and iron and barium nitrates co-impregnated samples are shown in Fig. 1(b and c), respectively. The weight loss in the range between 100 and 400 °C is attributed to the decomposition of iron nitrite, while the weight loss between 450 and 600 °C is perhaps due to the decomposition of $Ba(NO_3)_2$. Compared with the DTG profile of Ba/Al_2O_3, it is found that the decomposition peak corresponding to well dispersed $Ba(NO_3)_2$ nearly disappears and only the decomposition peak for bulk $Ba(NO_3)_2$ can be clearly observed, suggesting that the introduction of iron nitrate inhibits the dispersion of barium species. This can be confirmed by the XRD investigation shown in Fig. 2. From this figure, it is easily found that after drying at 120 °C, the diffracted peaks for $Ba(NO_3)_2$ phase are much stronger in Fe-Ba/Al_2O_3 than in Ba/Al_2O_3. After calcination at 600 °C, the XRD-visible $Ba(NO_3)_2$ phase decomposes into bulk BaO and readily reacts with the Al_2O_3 support, resulting in the formation of large $BaAl_2O_4$ particles [26]. Accordingly, the diffracted peaks for $BaAl_2O_4$ phase in Fe-Ba/Al_2O_3 are also sharper and higher than those in the Ba/Al_2O_3, as shown in Fig. 2(b).

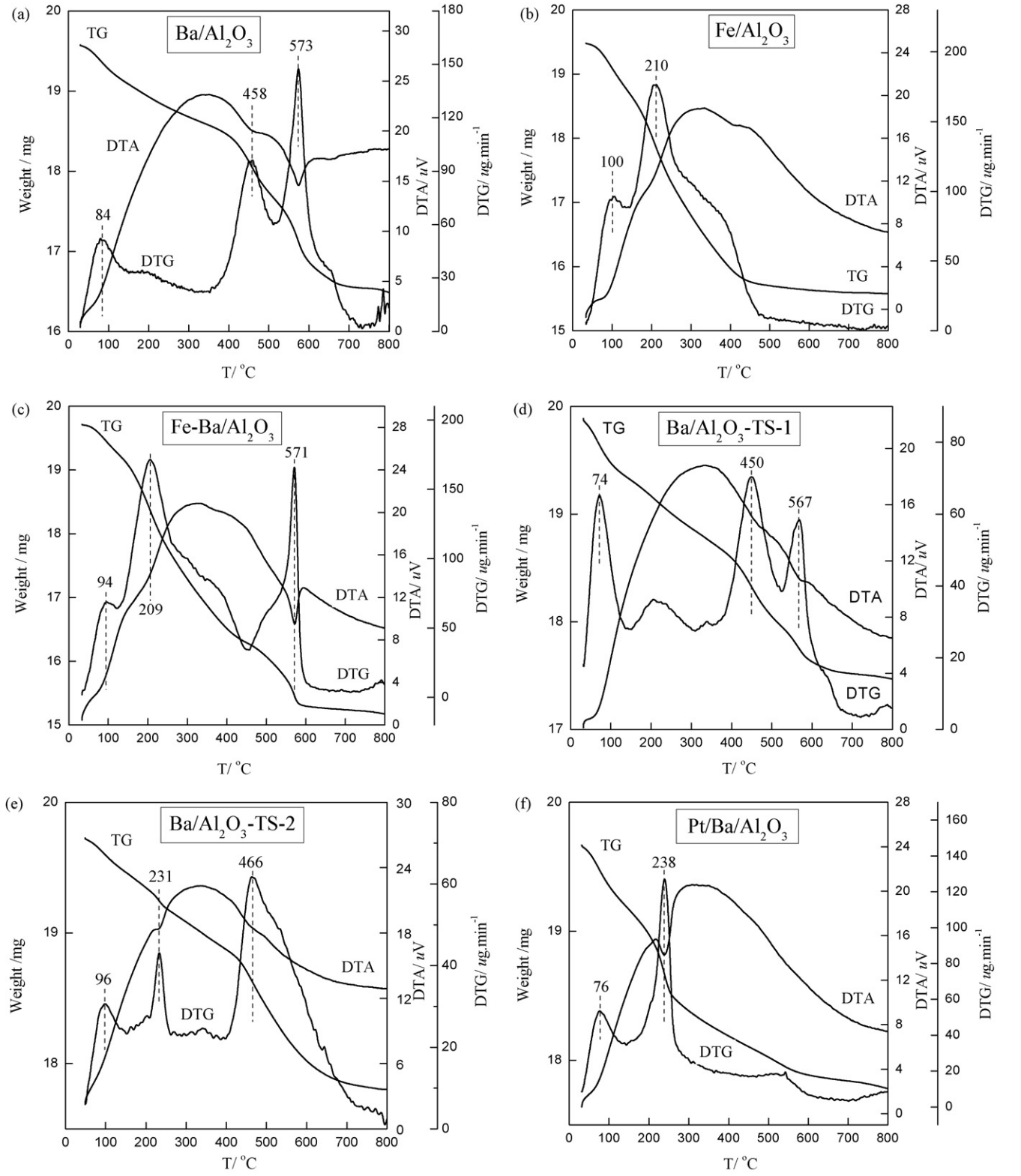

Fig. 1. The TG/DTA curves for the precursors: (a) $Ba(NO_3)_2$ impregnated on Al_2O_3; (b) $Ba(NO_3)_2$ and $Fe(NO_3)_3$ co-impregnated on Al_2O_3; (c) after the first impregnation step for $Ba(NO_3)_2$ on Al_2O_3 in the two-step sequential impregnation preparation; (d) after the second impregnation step for $Ba(NO_3)_2$ on Al_2O_3 in the two-step sequential impregnation preparation; (e) Pt deposited on Ba/Al_2O_3.

Fig. 1(d and e) give the TG-DTA profiles of sample Ba/Al_2O_3 during two-step sequential impregnation. Since the area of the peak at ca. 450 °C is much larger than that at 570 °C, the $Ba(NO_3)_2$ should mainly exist as well-spread barium species with high dispersion. As a result, no peak for barium-containing phase can be observed in the XRD pattern for the sample calcined at 600 °C. However, strong characteristic reflections for $BaAl_2O_4$ in $Fe/Ba/Al_2O_3$-TS are observed after further iron

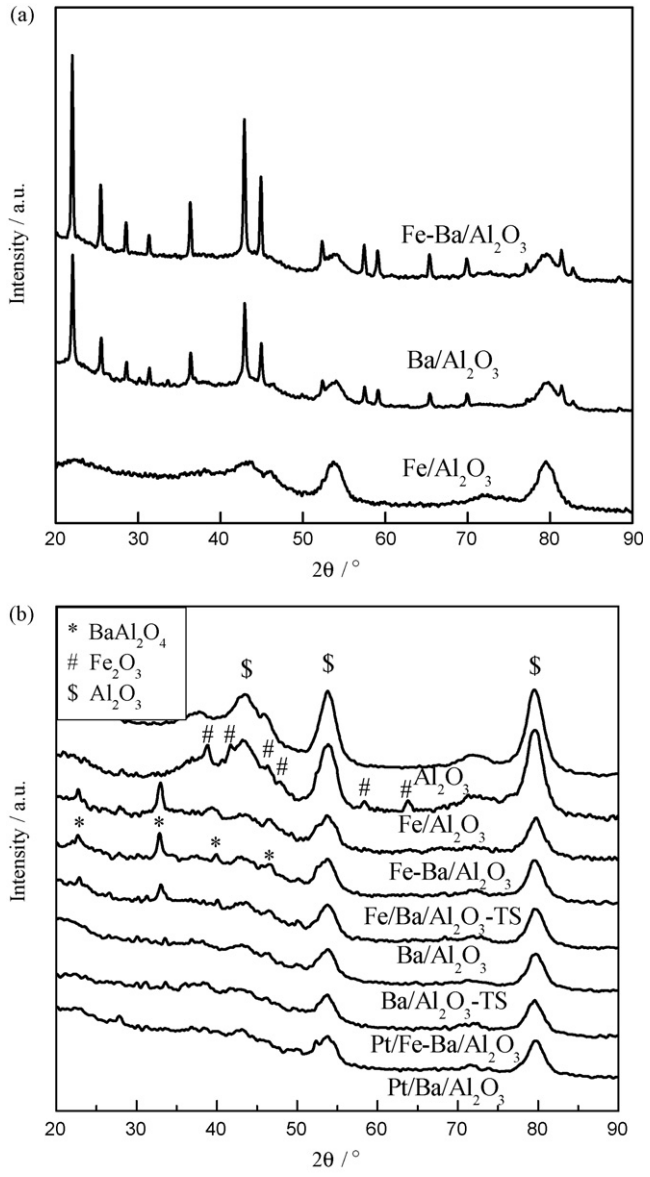

Fig. 2. The XRD patterns of the samples: (a) after drying at 120 °C and (b) after calcination at 600 °C.

impregnation, indicating that the presence of iron oxides induces the agglomeration of barium species. From the intensity of diffracted peaks for $BaAl_2O_4$, it can be inferred that the order of dispersion for barium species is Ba/Al_2O_3-TS > Ba/Al_2O_3 > $Fe/Ba/Al_2O_3$-TS > $Fe\text{-}Ba/Al_2O_3$.

It is strange that for the sample prepared by sequential impregnation method, the decomposition of bulk barium $Ba(NO_3)_2$ is found during the first impregnation step, but no corresponding $BaAl_2O_4$ phase can be detected in the XRD pattern. Worth noting that in Fig. 1(e) a sharp peak centered at 231 °C in the DTG curve appears during the second impregnation step which was never observed before. Also, in Fig. 1(f) a sharp peak at 238 °C can be observed for the Pt-impregnated Ba/Al_2O_3 sample. The Pt-impregnated $Fe\text{-}Ba/Al_2O_3$ exhibits a similar peak at 248 °C (figure not shown). Casapu et al. [27] ever reported that the $Pt/BaAl_2O_3$-BaO/Al_2O_3 sample treated with water was amorphous in XRD measurement due to the hydrolyzation of $BaAl_2O_4$ by water, and no characteristic pattern for the hydrates can be identified. On this basis, the sharp endothermic peak centered at ca. 230–250 °C should be related to the evolution of water in the hydrate, possibly in the form of $BaO{\cdot}Al_2O_3{\cdot}H_2O$ as deduced from the temperature of dehydration [27]. After dehydration, the barium species seem to undergo a redistribution process since the Ba-related phase totally disappears in Ba/Al_2O_3-TS and Pt-containing catalysts as shown in Fig. 2(b), suggesting that the XRD-visible $BaAl_2O_4$ phase has transformed into amorphous state. Although some studies [28,29] indicated that the small $BaAl_2O_4$ crystallites are favorable to NO_x trapping, the large $BaAl_2O_4$ crystals are believed to have a negative effect on the NO_x storage performance, mainly due to the diffusion limitation of absorbed nitrates, which has been also confirmed by our results in Section 3.2. Here the described $BaAl_2O_4$ phase transformation upon water treatment gave rise to the re-dispersion of barium species, and this phenomenon may hold great promise for regeneration of thermally aged NSR materials.

3.2. NO_x storage

3.2.1. NO_x storage behaviors

Fig. 3 presents NO_x storage results at 300 °C as the feed gas is switched to pass through the catalyst bed. The NO_x breakthrough profiles shown in Fig. 3(a) for Pt-free catalysts can be divided into two periods, a fast increase in NO_x concentration in the first ca. 1000s and a subsequent slow increase afterwards. During the first period, the sample Ba/Al_2O_3-TS shows the highest NO_x storage efficiency as indicated by the lowest NO_x concentration, followed by the sample Ba/Al_2O_3, while the Fe-containing catalysts have the lowest NO_x trap efficiency. This trend correlates very well with the dispersion state of barium species as analyzed in Section 3.1. Normally, the higher the dispersion of the barium species, the faster NO_x-storing rate is. During this period, the NO_x is thought to be stored on the highly dispersed barium species, mainly the surface barium sites. The second storage period corresponds to the slow diffusion of the surface NO_x into the bulk or semi-bulk storage phase, and saturation is not reached even after 6000 s storage.

The results of calculated NO_x storage capacities for catalysts from Fig. 3 are listed in Table 1. It can be seen that the catalysts prepared by sequential impregnation exhibit slightly larger NO_x storage capacities than those by one step impregnation, probably due to higher dispersion of barium species in Ba/Al_2O_3-TS. Surprisingly, the Fe-containing catalysts have higher NO_x storage capacity, when compared with the Ba/Al_2O_3 catalyst, although Fe contributes to agglomeration of barium species. After the introduction of Fe to Ba/Al_2O_3-TS, the NSC is increased by 26% from 186 to 226 μmol/g, indicating that iron oxide has a positive effect on the amounts of NO_x storage.

Fig. 4 shows the XRD patterns of the samples before and after NO_x storage. From this figure, it is found that the diffracted peaks for $BaAl_2O_4$ remain nearly unchanged and no NO_x-related species like $Ba(NO_3)_2$ can be detected in Ba/Al_2O_3

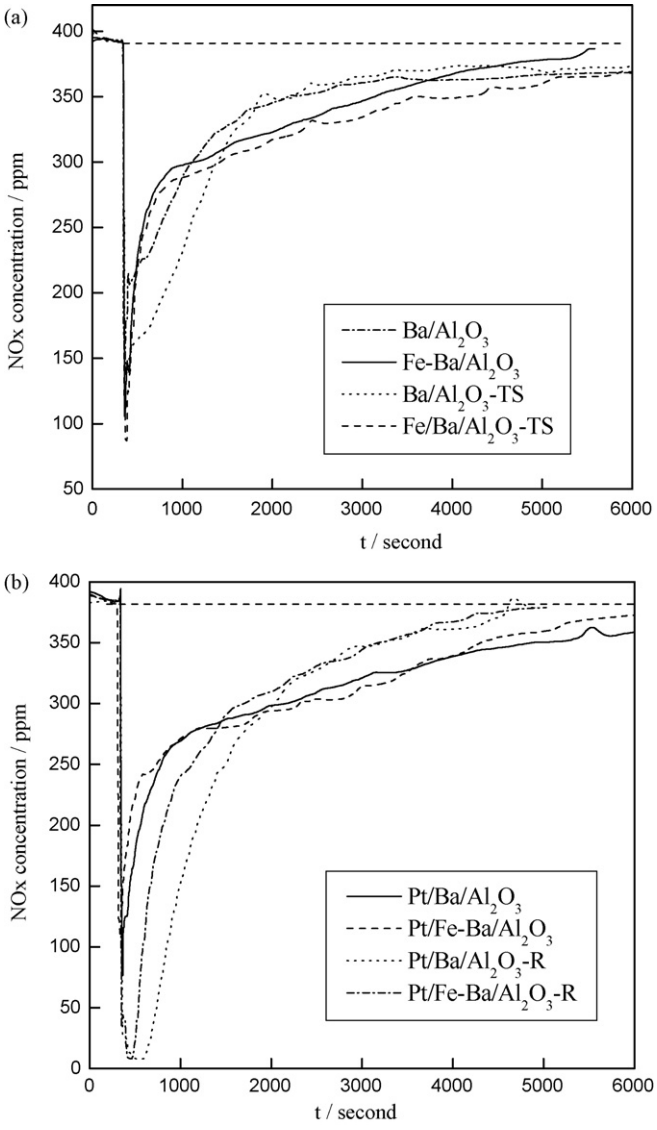

Fig. 3. The NO_x storage profiles of NSR catalysts: (a) Ba/Al_2O_3 and Fe-Ba/Al_2O_3; (b) fresh and reduced Pt-containing catalysts.

catalyst, indicating that NO_x is mainly stored on the surface sites of the catalysts but not in the bulk barium species. In contrast, the Fe-containing catalysts contain $Ba(NO_3)_2$ crystallites after storage, especially for the sample $Fe/Ba/Al_2O_3$-TS. After NO_x storage, the XRD pattern of this catalyst shows very obvious diffracted peaks of $Ba(NO_3)_2$ phase,

Table 1
NO_x storage capacities on NSR catalysts

Sample	NO_x storage capacities ($\mu mol/g^{-1}$)
Ba/Al_2O_3	163
Ba/Al_2O_3-TS	186
Fe-Ba/Al_2O_3	179
$Fe/Ba/Al_2O_3$-TS	226
$Pt/Ba/Al_2O_3$	267
$Pt/Ba/Al_2O_3$-R	306
Pt/Fe-Ba/Al_2O_3	245
Pt/Fe-Ba/Al_2O_3-R	239

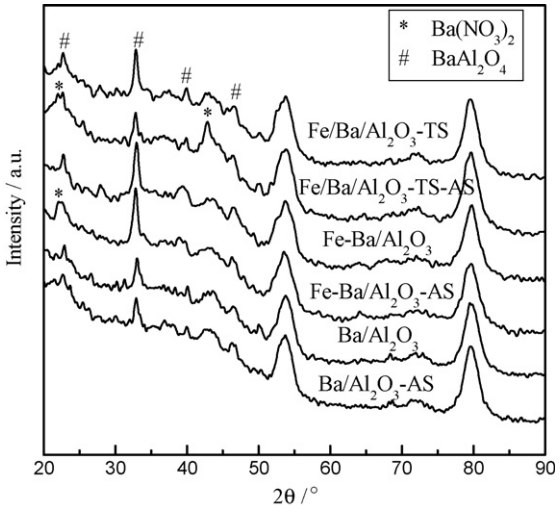

Fig. 4. The XRD patterns of the catalysts before and after storage (AS).

accompanying a consequent decrease in the peak intensity of $BaAl_2O_4$ phase, meanwhile, no Fe-containing species are detected, suggesting that Fe species do not store NO_x themselves, but promote the diffusion and mobility of stored NO_x, making the semi-bulk and bulk $BaAl_2O_4$ partly serve as storage phase. This is very similar to the findings of Klabunde group [30–36]. They reported repeatedly the beneficial effect of a surface-coating Fe_2O_3 layer on the absorption capacity of alkaline-earth oxides (MO) as absorbents for environmental toxins, like chlorinated hydrocarbons and acid gases (SO_2, H_2S, COS, CS_2). In these absorbents, the Fe_2O_3 generally enhances the use of the inner layer or the bulk-like part of MO during absorption, possibly due to the enhanced mobility of the absorbed species, while it exists always as iron oxide during the whole process. In our case, the mechanism for the storage of NO_x, also an acid gas, may be similar to the acid gas absorbed on the Fe_2O_3-coated MO, where iron oxide decreases the diffusion resistance and promotes the mobility of the stored NO_x.

The fresh Pt-promoted catalysts display similar storage profiles with the Ba/Al_2O_3 and $FeBa/Al_2O_3$ catalysts as shown in Fig. 3(b), but the addition of Pt enhances the NSC to a great extent, probably due to the high catalytic activity of Pt for NO oxidation to NO_2, which is generally considered as the first and a crucial step for NO_x storage [37]. However, the higher dispersion of barium species induced by the impregnation of $H_2PtCl_6{\cdot}6H_2O$ solution cannot be disregarded as well. After reduction pretreatment, a period of complete NO_x uptake can be observed for the Pt-containing catalysts. It means that Pt in metallic state can adsorb and oxidize NO to NO_2 much more quickly. As a result, the reduced $Pt/Ba/Al_2O_3$ shows a NSC of 306 μmol/g, which is about 15% higher than that for the fresh $Pt/Ba/Al_2O_3$ catalyst. Worth noting that after reduction pretreatment, although a complete NO_x storage can still be observed, the NSC for the sample Pt/Fe-Ba/Al_2O_3 does not increase but drops a little. This is related to the component interaction and will be discussed in Section 3.4.3.

3.2.2. DRIFTS study of NO_x adsorption

The DRIFTS experiments were carried out for figuring out the storage pathways. Both NO/He and NO/air adsorption were performed. The results are shown in Fig. 5. The appearance of negative bands is related to the decomposition of surface carbonates or their transformation to nitrites or nitrates during storage process. The analysis results show that only trace amount of surface nitrites (weak band at 1230 cm^{-1}) are formed upon NO/He admission at 300 °C on the Ba/Al_2O_3 and $Fe/Ba/Al_2O_3$ catalysts (figures not shown), where NO is bonded to the surface lattice oxygen of barium species by N atom [12]. Different results are obtained in case of NO adsorption on $Pt/Ba/Al_2O_3$-R as shown in Fig. 5(a). At short exposure time (10 min), very small amount of surface nitrites are formed (weak band at 1229 cm^{-1}). At longer exposure times, this band stabilizes in intensity. In parallel, characteristic bands of ionic nitrates at 1320 and 1420 cm^{-1} [7] develop gradually. Combined the results with those of NO adsorption on Ba/Al_2O_3, it can be deduced that the surface nitrates originate from the slow oxidation of the surface barium nitrites species, which can serve as an intermediates for NO storage on $Pt/Ba/Al_2O_3$. Since no gas phase O_2 was introduced, the oxygen required for oxidation most probably originates from the dissociation of NO molecule on metallic Pt sites. The atomic oxygen can oxidize surface nitrites to ionic nitrates through oxygen spillover on the support.

The DRIFTS spectra recorded on admission of NO/air mixtures over Ba/Al_2O_3 at 300 °C are similar to those on admission of NO/He, suggesting that the gas phase O_2 could not oxidize surface nitrites to nitrates species. But NO/air admission generates appreciable change in the DRIFTS spectra on $Fe\text{-}Ba/Al_2O_3$. Minor amount of surface barium nitrites (1230 cm^{-1}) are formed very quickly upon exposure to NO/air. At longer exposure time this band reaches maximum, and bands due to bidentate nitrates (1303 cm^{-1}) [7] and ionic nitrates (1324 cm^{-1}) develop obviously. It can be seen that surface nitrites are formed prior to nitrates species, suggesting that NO/air storage on $Fe\text{-}Ba/Al_2O_3$ at 300 °C experiences a nitrite route as well, similar to NO adsorption on $Pt/Ba/Al_2O_3$. However, some differences still exist, in $Fe\text{-}Ba/Al_2O_3$ sample, NO_x is mainly stored as bidentate type nitrates, while in $Pt/Ba/Al_2O_3$ mainly as ionic nitrates. The differences in the oxidation products may arise from the different oxidation performance of Pt and iron oxide. Pt can dissociate NO and generate highly reactive atomic oxygen, which can spill over through the support onto the surface nitrites sites, probably for a distance of

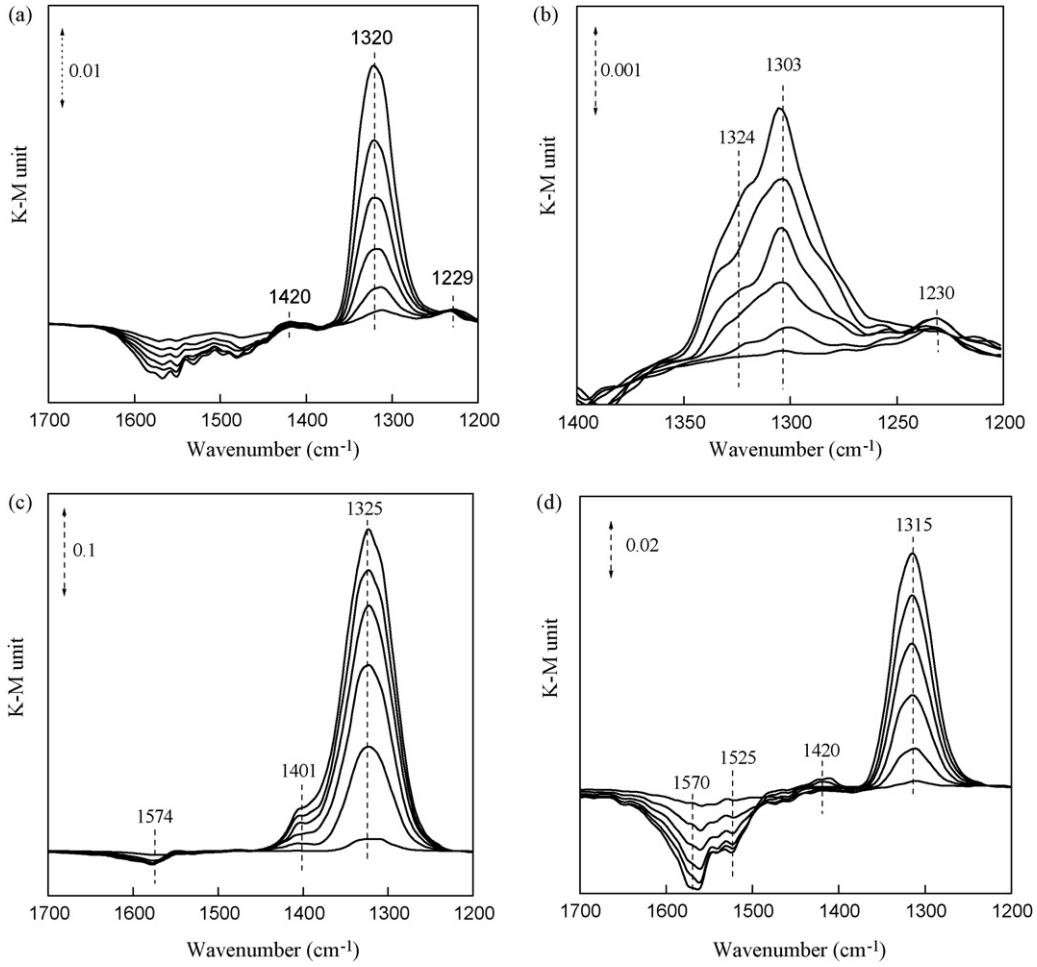

Fig. 5. The DRIFTS spectra of NO adsorption on the samples: (a) NO adsorption over $Pt/Ba/Al_2O_3$-R; (b) NO/air adsorption over $Fe\text{-}Ba/Al_2O_3$; (c) NO/air adsorption over $Pt/Ba/Al_2O_3$; (d) NO/air adsorption over $Pt/Fe\text{-}Ba/Al_2O_3$. The spectra were recorded every 10 min till an hour after exposure to NO_x.

a few micrometers [38]; whereas, it is well established that metal oxide like Fe_2O_3 can hardly dissociate the gas phase oxygen into atomic oxygen, the oxidation of nitrites into nitrates takes place only on the sites that are in close contact with iron oxide.

DRIFTS spectra on adsorption of NO/air at 300 °C over reduced Pt/Ba/Al_2O_3 and Pt/Fe-Ba/Al_2O_3 catalysts at different exposure time are displayed in Fig. 5(c and d), respectively. Very strong bands due to ionic nitrates are clearly visible, while no surface nitrites can be observed, suggesting that NO_x is not stored by the nitrites route. It is well known that the noble metal Pt is highly active for the oxidation of NO to NO_2, especially at temperature above 250 °C [39]. It has been also reported [7,10] that NO_2 can be directly stored on Ba/Al_2O_3 as ionic nitrates without nitrites formation. On this basis, NO_x storage on these Pt-containing catalysts in presence of O_2 starts from the oxidation of NO to NO_2.

It can be seen from the band intensity that the NO_2 route is a more efficient way to store NO_x than the nitrite route. Since the introduction of Pt produces a higher dispersion of barium species during preparation, one might think that the promotion in NSC results from the Pt-induced re-dispersion of barium species. Actually, the oxidation ability of Pt plays a more important role in the storage process. For example, the barium species in Ba/Al_2O_3-TS and Pt/Ba/Al_2O_3-R are both highly dispersed as indicated by XRD characterization, but the Pt/Ba/Al_2O_3-R catalyst exhibits a NSC, about 1.65 times larger than the Ba/Al_2O_3-TS catalyst. It does not seem that the dispersion of barium species plays an important role in the amount of NO_x stored. It is more likely that the storage routes, which depend on the feed gas and catalyst composition, determine the NSC of the sample.

3.3. Sulfation and desulfation

3.3.1. FT-IR and XRD

Fig. 6 shows the normalized FT-IR spectra of catalysts after sulfation. The band at 1634 cm^{-1} is due to adsorbed water and the peak at 1385 cm^{-1} is assigned to trace amount of undecomposed nitrates, whereas bands at 1402 and 1442 cm^{-1} can be attributed to surface unidentate carbonates [40]. Furthermore, peaks at 981 and 1121 cm^{-1} in addition to two shoulders at 1085 and 1185 cm^{-1} reveal the presence of bulk sulfate [40]. Liu and Anderson [41] thought that the presence of Pt is required for bulk barium sulfate formation, while Abdulhamid et al. [14] reported that Pt does not appear to play an essential role for sulfate formation. The results here clearly show that Pt is not necessarily required for the formation of sulfate, but the presence of Pt promotes the SO_x adsorption, since the Pt-containing catalysts always show bands of sulfate in much higher intensity. This can be confirmed by the XRD patterns shown in Fig. 7. All these samples exhibit characteristic pattern for $BaSO_4$ clearly, but the Pt-containing catalysts contain larger amounts of $BaSO_4$, which can be seen from the higher intensity of XRD patterns for these samples. Furthermore, the introduction of iron has a pronounced effect on decreasing the $BaSO_4$ particle size when compared the peak

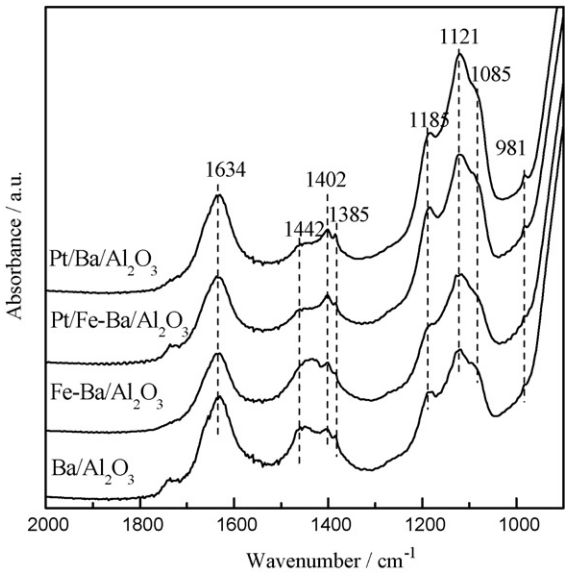

Fig. 6. The FT-IR spectra of the catalysts after sulfation.

width at half maxima (PWHM) of the corresponding peak at $2\theta = 50^\circ$ (marked by an arrow) for Fe-containing catalysts with that for Fe-free catalysts. However, there is little change in the intensity of $BaAl_2O_4$ before and after sulfation, suggesting that large $BaAl_2O_4$ particles are inactive for SO_x absorption. After sulfation, two diffracted peaks for Pt can be observed at $2\theta = 46.4^\circ$ and 54.2°, which indicates that the sulfation can induce the reduction of Pt to metallic state. This can be also confirmed by the color change from white for the fresh sample into gray after sulfation. This sulfation-induced reduction phenomenon is also observed in the sulfation process of Pt/Al_2O_3 catalyst [42].

3.3.2. TPR

TPR measurements were performed for the quantitative investigation of the sulfur poison and regeneration of the catalysts. Fig. 8 shows the TPR profiles of the catalysts before

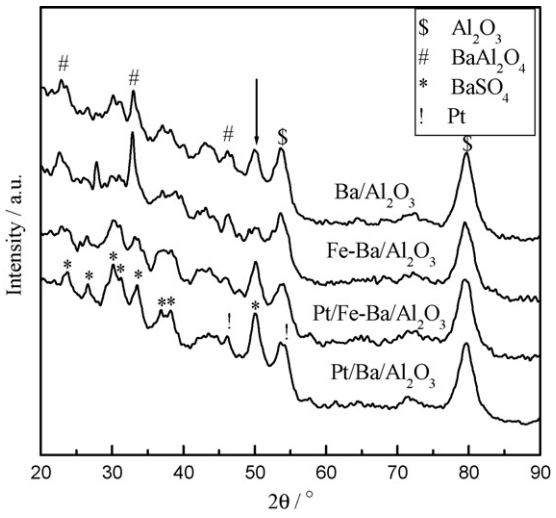

Fig. 7. The XRD patterns of the catalysts after sulfation.

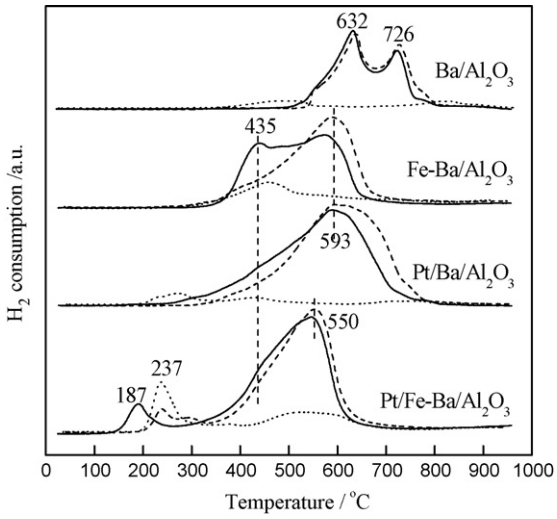

Fig. 8. The TPR profiles of the catalysts pretreated at different conditions, (···) before sulfation, (—) after sulfation at 400 °C, (- - -) after sulfation at 400 °C followed by oxidation at 600 °C in 6% O_2/He flow.

and after sulfation at 400 °C, as well as further oxidation at 600 °C.

It can be seen from the fresh Pt/Ba/Al_2O_3 catalyst that the broad peak between 200 and 300 °C is assigned to reduction of platinum oxide. A much higher peak is observed at 237 °C for fresh Pt/Fe-Ba/Al_2O_3, which can be attributable to the reduction of both platinum oxide and iron oxide. Compared with the reduction peak of iron oxide at 435 °C in Fe-Ba/Al_2O_3, the reduction temperature for iron oxide in Pt/Fe-Ba/Al_2O_3 is decreased by almost 200 °C, which is due to the spillover-hydrogen generated by Pt. The reduction of iron oxide is further promoted after sulfation, with the reduction peak occurring only at 187 °C. Since XRD results have confirmed that the platinum oxide is reduced to metallic Pt after sulfation, the reduced Pt metal can directly dissociate H_2 and promote the reduction of iron oxide, but for catalyst without sulfation, platinum species need to be reduced firstly at above 200 °C.

The peak at 435 °C is attributed to the reduction of aluminum sulfate [43] and the peaks above 500 °C to the reduction of barium sulfates. It can be seen that the iron oxide has great ability for deposition of sulfur on alumina support as aluminum sulfate. But after heating at 600 °C, aluminum sulfate is converted into more stable barium sulfates in Fe-Ba/Al_2O_3 catalyst. Absence of aluminum sulfate is observed in sulfated Ba/Al_2O_3 since no oxidation components are present (Pt, iron oxide) for SO_2 oxidation.

Two kinds of viewpoints concerning the presence state and reduction behaviors of $BaSO_4$ have been presented. Wei et al. [43] reported that two types of $BaSO_4$ were found—small particle size $BaSO_4$ (~3 nm) which is reducible at low temperatures, and large crystalline $BaSO_4$ (>10 nm) which is reducible at relatively higher temperatures, while Elbouazzaoui et al. [25] thought that the "surface" sulfates reduced at relatively low temperature are sulfates close to platinum, and the "bulk" sulfates reduced at high temperature are sulfates not proximal to platinum. The results here clearly indicate that the reduction of $BaSO_4$ depends on both the particle size and types of transition metals. Two reduction peaks in Ba/Al_2O_3 can be attributed to $BaSO_4$, probably with different particle size. After introduction of Pt or Fe, the reduction of $BaSO_4$ is predominantly promoted to 593 °C, mainly due to the atomic hydrogen generated by the reduced Pt or Fe metal. Worth noting that $BaSO_4$ is reduced at the lowest temperature 550 °C in sulfated Pt/Fe–Ba/Al_2O_3 catalyst, indicating that co-existence of Pt and Fe shows a synergistic effect on the reduction of $BaSO_4$. This should be resulted from the combinational effect of Fe and Pt on the decrease of the particle size of $BaSO_4$ and the supply of active spillover hydrogen.

Table 2
Calculated sulfur content from TPR test for catalysts after sulfation

Catalyst	S (wt%)
Ba/Al_2O_3	1.7
Fe-Ba/Al_2O_3	1.6
Pt/BaAl_2O_3	3.5
Pt/Fe-Ba/Al_2O_3	3.1

Since the sulfur-containing reduction products of sulfates by H_2 mainly consist of H_2S and BaS [25,44,45], and the presence of sulfides have been confirmed by XPS analysis (figures not shown), the stoichiometry of H_2/S should be equal to 4. So the sulfur content for these catalysts can be quantitatively calculated using CuO for calibration. The results are presented in Table 2. It can be seen that the introduction of Pt doubles the amounts of sulfur absorbed, consistent with the XRD and FT-IR results that much higher intensity corresponding to sulfates were observed in the Pt-containing catalysts. Although the introduction of Fe greatly inhibits the growth of sulfates, it only slightly decreases the sulfur content.

Repeated TPR tests were performed in order to investigate the extent of desulfation. After each reduction test to 600 °C and holding for 15 min, catalysts were reoxidized in 6% O_2/He flow at 600 °C for 1 h for complete oxidation of sulfides into sulfates. The TPR profiles are presented in Fig. 9 and the sulfur content is calculated and listed in Table 3. It can be seen that most of the sulfur (3 wt%) has been reduced for both Pt/Ba/Al_2O_3 and Pt/Fe-Ba/Al_2O_3 catalysts during the first TPR run, but they show different extent of desulfation. 2.3 wt% sulfur has been removed for Pt/Ba/Al_2O_3 catalyst after the first TPR run, accounting for 75% of the sulfur that has been reduced, and the sulfur continues to be removed in the second TPR cycle.

Table 3
Calculated sulfur amounts from TPR test for catalysts after different treatments

Pretreatments	Pt/Ba/Al_2O_3	Pt/Fe-Ba/Al_2O_3
TPR (a, 950 °C): sulfation	3.5	3.1
TPR (b, 600 °C, 15 min): sulfation	3.1	3.0
TPR (c, 600 °C, 15 min): TPR (b) + reoxidized 600 °C	0.8	2.6
TPR (d, 600 °C, 15 min): TPR (c) + reoxidized 600 °C	0.5	2.5
TPR (e): H_2/CO_2 (550 °C, 1 h) + reoxidized 600 °C	1.6	2.3

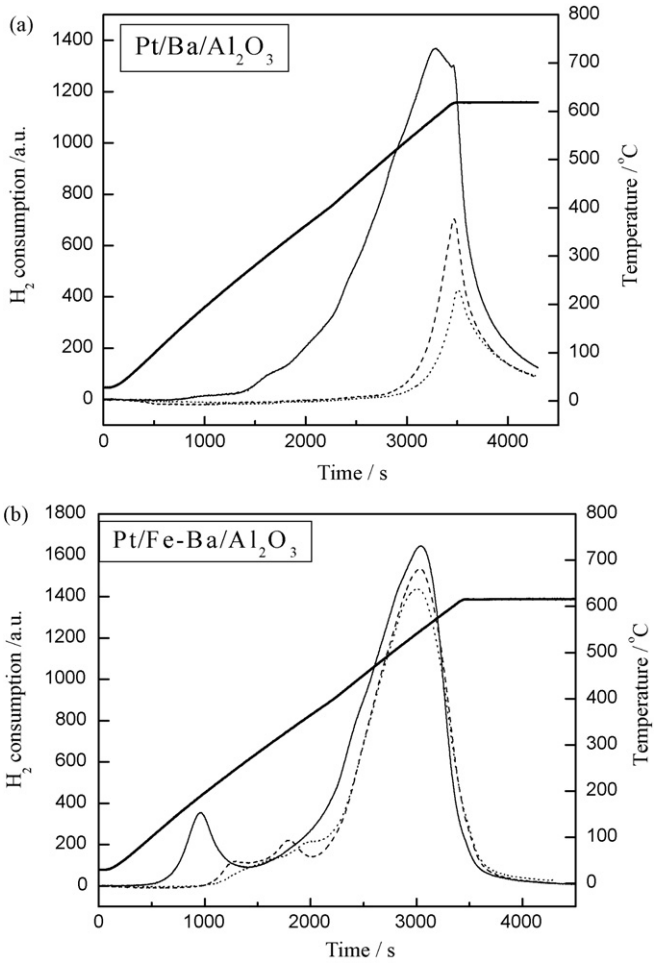

Fig. 9. The repeated TPR profiles of the catalysts $Pt/Ba/Al_2O_3$ (a) and $Pt/Fe\text{-}Ba/Al_2O_3$ (b), (—) the first cycle, (- - -) the second cycle, (· · ·) the third cycle. *The catalysts after TPR test were reoxidized in 6% O_2/He flow at 600 °C for 1 h for the next TPR cycle.

However, it is rather difficult to remove the sulfur in the $Pt/Fe\text{-}Ba/Al_2O_3$ catalyst. During the first TPR run, only 0.4 wt% sulfur is removed, while almost no sulfur is removed during the second TPR run. The amount of residual sulfur in $Pt/Fe\text{-}Ba/Al_2O_3$ after two repeated TPR tests are much higher than that in $Pt/Ba/Al_2O_3$. Since the sulfur-containing products mainly consist of H_2S and BaS for the reduction of barium sulfates by using H_2, it can be inferred from these results that $BaSO_4$ is reduced mainly through H_2S pathway in sulfated $Pt/Ba/Al_2O_3$ sample, while through BaS pathway in sulfated $Pt/Fe\text{-}Ba/Al_2O_3$ sample. The reaction pathways are shown as Eqs. (R_1) and (R_2). We calculated the reaction Gibbs function ΔG^{θ} of these equations at each temperature using HSC chemistry software and the results are shown in Table 4. Although thermodynamics does not give any information on kinetics of reactions, but they can give indications about the reaction that are favored at each temperatures. It can be seen that the BaS pathway occurs at much lower temperature than the H_2S pathway. Although $BaSO_4$ particle get reduced at lower temperature in $Pt/Fe\text{-}Ba/Al_2O_3$ than in $Pt/Ba/Al_2O_3$ due to the small sizes, it does not seem that the reduction temperature determines the reduction pathway. From Fig. 9(a) for $Pt/Ba/Al_2O_3$, it can be seen that the $BaSO_4$ that is reduced at low temperature is almost completely removed, but is relatively hard to remove for $BaSO_4$ that is reduced at high temperature. It is more likely that the component interaction governs the pathways for the reduction of $BaSO_4$.

$$BaSO_4 + 4H_2 = Ba(OH)_2 + H_2S + 2H_2O \quad (R1)$$

$$BaSO_4 + 4H_2 = BaS + 4H_2O \quad (R2)$$

$$BaSO_4 + CO_2 + 4H_2 = BaCO_3 + H_2S + 3H_2O \quad (R3)$$

Since CO_2 is always present in the exhaust and it has been reported that $BaCO_3$ can replace BaS during regeneration [46] which will contribute to sulfur removal, another possible pathway for $BaSO_4$ reduction is proposed as shown in Eq. (R_3). It can be seen from the results shown in Table 4 that this reaction is always thermodynamically favorable in the entire temperature range from 0 to 800 °C. So the sulfated samples were treated in the reducing gas (H_2/N_2) by introducing 10 vol%CO_2 at 550 °C for 1 h. The results are shown in Table 3 as TPR (e). Even if the performed reduction temperature is lowered by 50 °C as compared with that in TPR run by using H_2 only, more sulfur was removed in $Pt/Fe\text{-}Ba/Al_2O_3$ when CO_2 is present, indicating the positive effect of CO_2 on catalyst desulfation by replacing BaS with $BaCO_3$. However, the sulfur content in $Pt/Fe\text{-}Ba/Al_2O_3$ is still higher than that in $Pt/Ba/Al_2O_3$ by 0.7%.

3.4. Components interactions and their effects on NO_x storage and desulfation

3.4.1. EXAFS

Now, there are still questions remaining as mentioned above, why $Pt/Ba/Al_2O_3$ and $Pt/Fe\text{-}Ba/Al_2O_3$ show different behaviors for NO_x storage after reduction pretreatment, and different extent of desulfation by using H_2 as reducing gas? It is generally believed that Pt is a key component for the oxidation and regeneration of the NSR catalysts, and the introduction of another metal may have a great influence on its presence and

Table 4
Thermodynamic calculation results (ΔG^{θ}, kJ/mol) of the reactions

	T (°C)								
	0	100	200	300	400	500	600	700	800
R_1	13.0	9.6	6.6	4.0	1.7	−2.9	−7.7	−12.6	−17.7
R_2	4.1	−13.5	−29.9	−45.3	−59.8	−73.6	−86.8	−99.5	−111.7
R_3	−99.8	−101.1	−101.4	−100.8	−99.6	−98.0	−96.0	−93.9	−91.7

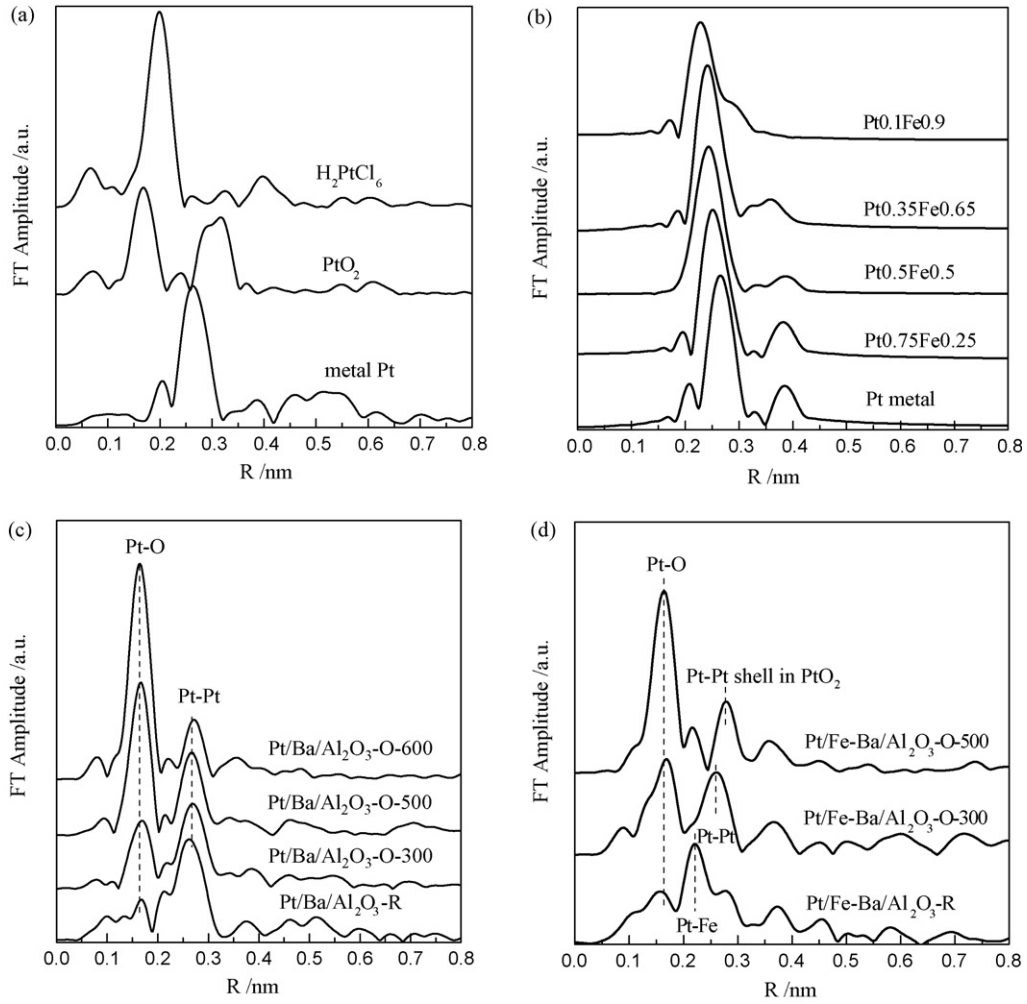

Fig. 10. The RSFs of Pt L-III edge: (a) the standard samples; (b) the theoretically simulated Pt–Fe alloys by Feff 8; (c) $Pt/Ba/Al_2O_3$ catalysts after different pretreatments; (d) $Pt/Fe\text{-}Ba/Al_2O_3$ catalysts after different pretreatments.

interaction with other components, like Ba species for storage. So it is highly necessary for us to investigate the state of Pt. Thus, EXAFS, as a powerful tool to study the highly dispersed species, was applied for the characterization of Pt under different pretreatments. The radial structural functions (RSFs) are displayed in Fig. 10, and the structural parameters, obtained from best-fitting in reference to the model compounds (Pt and PtO_2), as well as the corresponding Debye–Wallar factor and Eo shift are listed in Table 5. The residual factor R is within 10%, suggesting the considerable reliability of the fitting procedures.

In Fig. 10(c), two coordination peaks, one at 0.165 nm for Pt–O shell and the other at 0.268 nm for metallic Pt–Pt shell, are clearly visible in $Pt/Ba/Al_2O_3$ sample. Even after reduction, small Pt–O coordination peak can still be observed. It is not likely for metallic Pt to get oxidized when exposed to air at room temperature, so the appearance of the Pt–O bond may be due to Pt species interacting strongly with the lattice oxygen from the support which is difficult to reduce. With the increase in the oxidation temperature, the metallic Pt gets oxidized gradually, as indicated by the development of the Pt–O coordination peak and the slow decrease of the Pt–Pt coordination peak. Whatever, a small amount of Pt in metallic state is still present even after oxidation at high temperature of 600 °C.

Appreciable changes have taken place for $Pt/Fe\text{-}Ba/Al_2O_3$ catalyst after various pretreatments as shown in Fig. 10(d). After reduction, a main coordination peak at 0.22 nm appears which is not assigned to any bond in the metal structure of Pt. Considering that iron oxide gets reduced at low temperature which is facilitated by the spillover-hydrogen from Pt, the metallic Pt and Fe may interact with each other and form an alloy, and the peak at 0.22 nm is probably due to the Pt–Fe bond in the alloy. Since the model Pt–Fe alloy can be hardly prepared, we performed the RSF simulation of the alloy particles with diameters about 12 nm for figuring out this by using FEFF 8 software. The parameters like unit cell, space group and atom position are referred to FindIT program [47]. The simulated results are shown in Fig. 10(b). It can be seen that the main coordination peak tends to shift to lower coordination distance with the increase in Fe content, which is due to the change of the surrounding atoms. By comparison with the simulated RSF for model alloys, the RSF of $Pt/Fe\text{-}Ba/Al_2O_3$ is very similar to the Pt0.1Fe0.9 alloy (atomic ratio, ICSD

Table 5
The calculated structural parameters for the nearest Pt–O and Pt–Pt shells from EXAFS data

Samples	Shell	N[a]	R (nm)[b]	$\Delta\sigma^2 \times 10^3$ (Å^2)[c]	ΔE_0 (eV)[d]
Pt foil	Pt–Pt	12.0	0.277	–	–
PtO_2	Pt–O	6.00	0.204	–	–
$PtBaAl_2O_3$-R	Pt–Pt	8.22	0.276	1.45	3.41
$Pt/Ba/Al_2O_3$-O-300	Pt–O	2.45	0.203	2.87	−1.49
	Pt–Pt	5.37	0.280	1.90	3.12
$Pt/Ba/Al_2O_3$-O-500	Pt–O	3.60	0.201	−0.89	−2.76
	Pt–Pt	3.61	0.279	−0.55	0.47
$Pt/Fe\text{-}Ba/Al_2O_3$-O-300	Pt–O	1.70	0.203	4.20	−1.65
	Pt–Pt	3.90	0.273	2.80	−0.23
$Pt/Fe\text{-}Ba/Al_2O_3$-O-500	Pt–O	3.97	0.199	0.79	−2.08

[a] N: coordination number.
[b] R: coordination distance.
[c] $\Delta\sigma^2$: Debye–Waller factor.
[d] ΔE_0: E_0 shift.

#103603); both of them have a coordination peak at about 0.22 nm and a shoulder at the right side. This indicates that Pt and Fe can form an alloy in $Pt/Fe\text{-}Ba/Al_2O_3$ catalyst after reduction treatment, and this alloy consists of a large fraction of Fe. Pt can be considered dissolved in the lattice of Fe metal since Fe atoms present in much larger amount than Pt in the catalysts. Additionally, a small peak at 0.16 nm corresponding to the Pt–O bond can be observed. After oxidation at 300 °C this Pt–Fe alloy transforms into iron oxide and platinum oxide, as well as metallic Pt. However, the metallic Pt has a smaller size than that in $Pt/Ba/Al_2O_3$-O-300, which can be seen from the comparison between the Pt–Pt coordination number 3.9 in $Pt/Fe\text{-}Ba/Al_2O_3$ and 5.4 in $Pt/Ba/Al_2O_3$. After oxidation at 500 °C, the metallic Pt–Pt coordination peak at 0.26 nm disappears and a new peak at 0.28 nm due to the second Pt–Pt shell in PtO_2 appears, suggesting the complete oxidation of Pt species at 500 °C.

Based on the EXAFS analysis, we proposed models for the presence of Pt in $Pt/Ba/Al_2O_3$ and $Pt/FeBa/Al_2O_3$ catalysts under different treatments as shown in Fig. 11. The Pt particles in $Pt/Ba/Al_2O_3$ present in considerable sizes after reduction, as indicated by the large coordination number of 8. It is believed that larger Pt particles are more oxidation-resistant since the oxidation of Pt starts from the surface to bulk, and therefore, a core–shell model can be built. Due to the diffusion limitation, metallic Pt is still present after oxidation at 600 °C. While in sample $Pt/Fe\text{-}Ba/Al_2O_3$-R the Pt and Fe form an alloy with a high Fe content, Pt atoms are atomically distributed in the

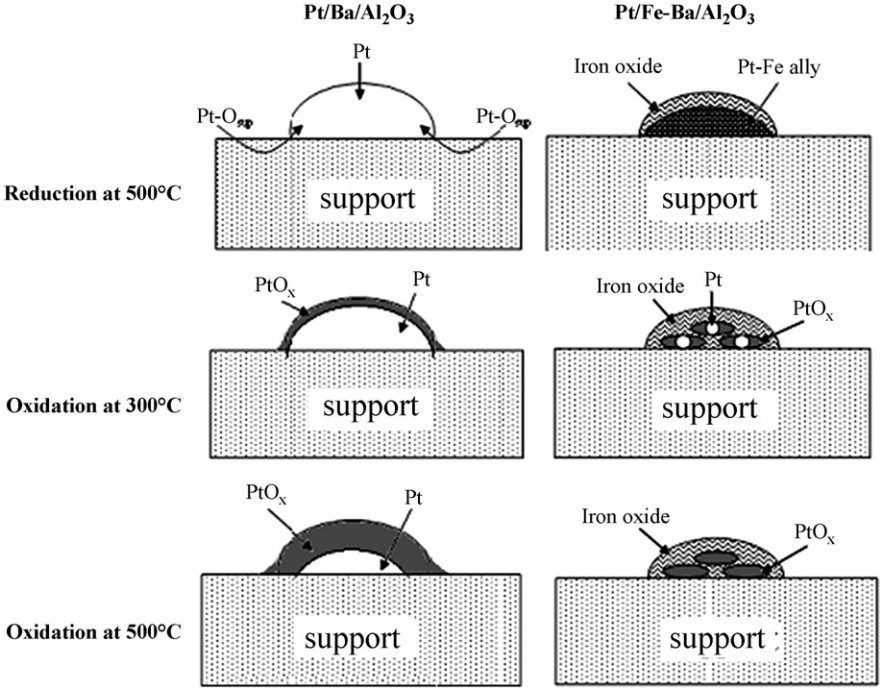

Fig. 11. A proposed model for the Pt state under different pretreatments.

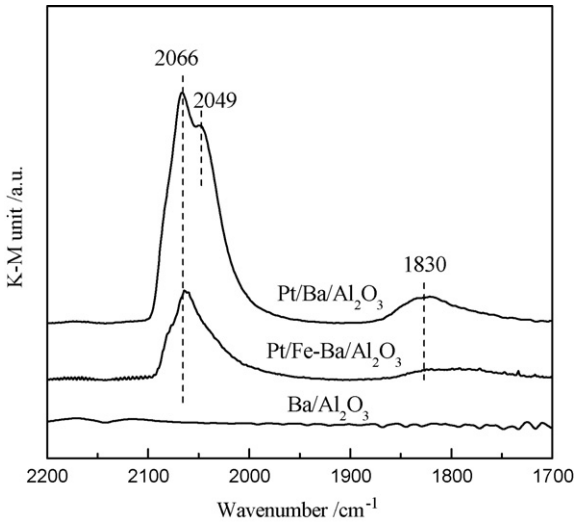

Fig. 12. The DRIFTS spectra of CO chemisorption over the different catalysts.

matrix of Fe lattice. These Pt species can be more easily oxidized due to the smaller size and close contact with the Fe/FeO_x. As a result, the complete oxidation of Pt into PtO_x occurs even at 500 °C.

3.4.2. DRIFTS of CO chemisorption

As Pt and Fe strongly interact with each other and form an alloy after reduction treatment, it is natural to think that the Pt sites may be covered by Fe or FeO_x under real operations. For figuring out this, DRIFTS of CO chemisorption on Ba/Al_2O_3, Pt/Ba/Al_2O_3 and Pt/Fe-Ba/Al_2O_3 after reduction were performed in order to probe Pt sites. The results are shown in Fig. 12. Both linear-CO (L-CO) and bridged-CO (B-CO) species were discernable on Pt/Ba/Al_2O_3 (L-CO at 2066 and 2049 cm^{-1}, and B-CO at 1830 cm^{-1}). Two L-CO bands indicate two kinds of Pt sites. As is known that the alkaline BaO/Al_2O_3 support is electron-rich, it will donate the electron density to the 5d orbit of Pt when Pt is supported [48]. As a result, Pt will have a larger potential to back-donate the electron density from its 5d orbit to CO ($2\pi^*$) when CO is chemisorbed, which will lead to the red shift in CO vibration. On this basis, the L-CO at 2049 cm^{-1} can be assigned to CO linearly adsorbed on Pt sites close to Ba species, and the other band at 2066 cm^{-1} assigned to CO chemisorbed on Pt in contact with Al_2O_3.

For Pt/Fe-Ba/Al_2O_3, the band at 2066 cm^{-1} can be assigned to the CO chemisorbed on Pt sites on the surface of the Pt–Fe alloy on the basis of EXAFS analysis. No band shift was observed for CO chemisorption on Pt–Fe alloy, as compared with that on Pt sites in contact with Al_2O_3. This is similar to CO chemisorption on reduced Pt/Al_2O_3 and PtFe/Al_2O_3 where negligible band shift can be observed [49]. The band at 2049 cm^{-1}, which is related to the CO adsorbed on the Pt sites close to Ba species, does not develop, suggesting that there are few Pt sites interacting with Ba species. Furthermore, the abundance of the L-CO and B-CO decreased to a great extent in Pt/Fe-Ba/Al_2O_3 by comparison with Pt/Ba/Al_2O_3, confirming that considerable amounts of Pt are encapsulated or covered by the Fe/FeO_x. In a similar Pt/Fe/Al_2O_3 catalyst [50], the Pt particles covered by a nano-layer of Fe_2O_3 can be clearly observed in TEM image.

3.4.3. Significance of Pt–Ba interaction for NO_x storage and desulfation

DRIFTS analysis has confirmed that NO_x is stored on Pt-containing catalysts via NO_2 route. Based on the analysis of DRIFTS of CO chemisorption, it seems that two types of platinum sites seem to operate during NO_x storage; the sites in contact with Al_2O_3 are responsible for NO_2 formation, while the other sites close to Ba species are active in barium nitrate formation, possibly via NO_2 spillover in the Pt–Ba interface. Mahzoul et al. [51] also found two kinds of Pt sites by using TPD technique. On this basis, it can be seen that the NO_x oxidation and subsequent spillover are two key steps for NO_x storage.

Although Fe can promote the NO_x diffusion in the bulk $BaAl_2O_4$ phase by increasing the mobility of the stored NO_x, its effect is unobvious during NO_x storage on Pt/Fe-Ba/Al_2O_3 since the bulk $BaAl_2O_4$ phase is re-dispersed by introduction of Pt. This is consistent with the findings that the Pt and Ba weight loading has a much greater effect than Fe weight loading on the performance of NSR catalysts [23]. In addition, the introduction of Fe lowers the NO oxidation rate due to the coverage of active Pt sites by Fe/FeO_x matrix and the formation of less active platinum oxide. What is more, the NO_2 spillover is greatly suppressed because of the absence of Pt–Ba interface after the introduction of Fe. Spillover of species between Pt and BaO is reported to be much faster when Pt and BaO are in close proximity [52]. Therefore, that the NSC is much lower in Pt/Fe-Ba/Al_2O_3 than in Pt/Ba/Al_2O_3 is natural, especially after reduction pretreatment.

The importance of Pt–Ba interaction is more clearly exhibited during the sulfur removal for the sulfated NSR catalysts. In sulfated Pt/Ba/Al_2O_3, most of the sulfate is reduced into H_2S during reduction, which contributes to the removal of sulfur. Although Pt is also present in Pt/Fe-Ba/Al_2O_3 catalyst, the Pt–Ba interaction is severely suppressed due to Pt–Fe alloy formation, leading to the reduction of $BaSO_4$ mainly as BaS. Considering the large amount of Fe and Ba in Pt/Fe-Ba/Al_2O_3, it is supposed that most of the Ba species are in close contact with Fe species. On this basis, we conclude that Fe and Pt selectively catalyze the reduction of $BaSO_4$ to different products: Fe catalyzes the reduction of $BaSO_4$ mainly into BaS, while Pt catalyzes it into H_2S. The sulfur can be removed from the catalysts via H_2S route, but it is difficult to remove via BaS route as the storage sites are still poisoned by repeated phase transformation between BaS and $BaSO_4$ under redox atmospheres. Therefore, the component interaction between Pt and Ba species is of great importance for the regeneration of NSR catalysts by selective removal of the sulfur as H_2S. Sakamoto et al. [38] reported that SO_x desoprtion occurs preferentially in an area only a few nanometers wide around the platinum, putting further evidence to the significance of Pt–Ba interaction. Kim et al. [53] investigated desulfation process over sulfated Pt/BaO/Al_2O_3 with different barium loading (8

and 20 wt%) and found that sulfur is more easily and completely removed in the sample with lower barium loading. They concluded that the morphology differences determine the extent of desulfation. From another point of view, the Pt–Ba interaction may play an important role. In the sulfated catalyst with high barium loading, most of the $BaSO_4$ is inaccessible to Pt sites since its formation is independent on the presence of Pt. Therefore, the sulfur within is difficult to remove. But in the sulfated catalyst with lower loading of barium, the barium sulfate has a greater probability to interact with the Pt species, facilitating the sulfur removal.

Although the introduction of Fe negatively influences the NO_x storage and sulfur removal efficiency due to the suppression of the Pt–Ba interaction, iron has positive effect on the inhibition in the growth of $BaSO_4$ particles, which may favor its reduction and regeneration of the NSC catalysts, especially in presence of CO_2. The key point is how to weaken the interaction between Pt and Fe. Recently, a physical mixture of powdery Fe_2O_3 and $Pt/Ba/Al_2O_3$ has been reported to be very effective for the NO_x purification in presence of SO_2 [20]. In this catalyst, the Pt is placed separately from iron species; it is not likely for the introduction of Fe to influence the Pt/Ba interaction. Thus the preparation method should play a great role in enhancing the Pt–Ba interaction and decreasing the Pt–Fe interaction.

4. Conclusions

(1) Two types of Ba species were identified on Ba/Al_2O_3 catalyst calcined at 600 °C, namely a well-spread monolayer Ba species and bulk $BaAl_2O_4$ crystallites. Bulk $BaAl_2O_4$ phase undergoes re-dispersion upon water treatment, which can be exploited as a potential application in regenerating the thermally deteriorated NSR catalysts.

(2) Two storage pathways exist for NO_x storage at 300 °C, including nitrite and NO_2 as intermediates, depending on the feed gas and catalyst composition. On $Fe\text{-}Ba/Al_2O_3$ catalyst, NO_x is stored through nitrite route in the presence of O_2, and Fe component promotes the diffusion of the stored-NO_x and the formation of bulk $Ba(NO_3)_2$, making the semi-bulk and bulk $BaAl_2O_4$ serve as storage phase; While on Pt-containing catalysts, NO_x is stored through NO_2 route in the present of O_2, which is more efficient than the nitrite route.

(3) The addition of Pt doubles the amounts of the absorbed sulfur and generates large $BaSO_4$ particles; the introduction of Fe not only slightly decreases the amount of absorbed sulfur, but also greatly suppresses the $BaSO_4$ particle size. The co-presence of Pt and Fe remarkably decreases the reduction temperature of $BaSO_4$ due to hydrogen spillover and smaller $BaSO_4$ particle size.

(4) Two kinds of Pt sites are present in $Pt/Ba/Al_2O_3$, including Pt close to Al_2O_3 and Pt interacted with Ba species. The interaction between Pt and Ba is important for NO_x spillover during storage and selective reduction of $BaSO_4$ to H_2S during sulfur removal. The introduction of Fe into the $Pt/Ba/Al_2O_3$ catalyst decreases the Pt–Ba interaction by encapsulation of Pt in the matrix of Fe/FeO_x lattice after redox cycle, leading to the decrease in the NO_x oxidation activity and spillover rate, as well as the increase in the difficulty for sulfur removal, since Fe selectively catalyzes the reduction of $BaSO_4$ into BaS.

Acknowledgements

This work is financially supported by the Natural Science Foundation of Tianjin of China (No. 05YFJMJC09700), the Specialized Research Fund for the Doctoral Program of Higher Education of China (No. 20040056028), the "863 Program" of the Ministry of Science & Technology of China (No. 2006AA06Z348) and the National Natural Science Foundation of China (No. 20676097). The authors are also grateful to the support of the Program of New Century Excellent Talents in University of China (NCET), the Program for Introducing Talents of Discipline to University of China (No. B06006) and the Program for Changjiang Scholars and Innovative Research Team in University of China (PCSIRT).

References

[1] S. Matsumoto, CATTECH 4 (2000) 102.
[2] R. Burch, J.P. Breen, F.C. Meunier, Appl. Catal. B Environ. 39 (2002) 283.
[3] H. Shinjoh, N. Takahashi, K. Yokota, M. Sugiura, Appl. Catal. B Environ. 15 (1998) 189.
[4] S. Matsumoto, Catal. Today 90 (2004) 183.
[5] L. Lietti, P. Forzatti, I. Nova, E. Tronconi, J. Catal. 204 (2001) 175.
[6] E. Fridell, M. Skoglundh, B. Westerberg, S. Johansson, G. Smedler, J. Catal. 183 (1999) 196.
[7] I. Nova, L. Castoldi, L. Lietti, E. Tronconi, P. Forzatti, J. Catal. 222 (2004) 377.
[8] Z. Liu, J.A. Anderson, J. Catal. 224 (2004) 18.
[9] Ch. Sedlmair, K. Seshan, A. Jentys, J.A. Lercher, J. Catal. 214 (2003) 308.
[10] F. Prinetto, G. Ghiotti, I. Nova, L. Lietti, E. Tronconi, P. Forzatti, J. Phys. Chem. B 105 (2001) 12732.
[11] C.M.L. Schole, V.R. Gangwall, M.H.J.M. de Croon, J.C. Schouten, J. Catal. 245 (2007) 215.
[12] P.J. Schmitz, R.J. Baird, J. Phys. Chem. B 106 (2002) 4172.
[13] P. Broqvist, I. Panas, H. Grönbeck, J. Phys. Chem. B 109 (2005) 9613.
[14] H. Abdulhamid, E. Fridell, J. Dawody, M. Skoglundh, J. Catal. 241 (2006) 200.
[15] P. Engström, A. Amberntsson, M. Skoglundh, E. Fridell, G. Smedler, Appl. Catal. B Environ. 22 (1999) L241.
[16] F. Basile, G. Fornasari, A. Grimandi, M. Livi, A. Vaccari, Appl. Catal. B Environ. 69 (2006) 59.
[17] H.Y. Huang, R.Q. Long, R.T. Yang, Appl. Catal. B Environ. 33 (2001) 127.
[18] J.M. Clacens, R. Montiel, H. Kochkar, F. Figueras, M. Guyon, J.C. Beziat, Appl. Catal. B Environ. 53 (2004) 21.
[19] S. Matsumoto, Y. Ikeda, H. Suzuki, M. Ogai, N. Miyoshi, Appl. Catal. B Environ. 25 (2000) 115.
[20] K. Yamazaki, T. Suzuki, N. Takahashi, K. Yokota, M. Sugiura, Appl. Catal. B Environ. 30 (2001) 459.
[21] P.T. Fanson, M.R. Horton, W.N. Delgass, J. Lauterbach, Appl. Catal. B Environ. 46 (2003) 393.
[22] R.J. Hendershot, W.B. Rogers, C.M. Snively, B.A. Ogunnaike, J. Lauterbach, Catal. Today 98 (2004) 375.
[23] R.J. Hendershot, R. Vijay, C.M. Snively, J. Lauterbach, Appl. Catal. B Environ. 70 (2007) 160.
[24] R.J. Hendershot, P.T. Fanson, C.M. Snively, J. Lauterbach, Angew. Chem. Int. Ed. 42 (2003) 1152.
[25] S. Elbouazzaoui, E.C. Corbos, X. Courtois, P. Marecot, D. Duprez, Appl. Catal. B Environ. 61 (2005) 236.

[26] T. Szailer, J.M. Kwak, D.H. Kim, J. Szanyi, C. Wang, C.H.F. Peden, Catal. Today 114 (2006) 86.
[27] M. Casapu, J.D. Drunwaldt, M. Maciejewski, M. Wittrock, U. Göbel, A. Baiker, Appl. Catal. B Environ. 63 (2006) 232.
[28] X. Li, M. Meng, P. Lin, T. Hu, Y. Xie, J. Zhang, Topic Catal. 22 (2003) 111.
[29] G. Zhou, T. Luo, R.J. Gorte, Appl. Catal. B Environ. 64 (2006) 88.
[30] S. Decker, K.J. Klabunde, J. Am. Chem. Soc. 118 (1996) 12465.
[31] C.L. Carnes, K.J. Klabunde, Chem. Mater. 14 (2002) 1806.
[32] Y. Jiang, S. Decker, C. Mohs, K. Klabunde, J. Catal. 180 (1998) 24.
[33] S.P. Decker, J.S. Klabunde, A. Khaleel, K.J. Klabunde, Environ. Sci. Technol. 36 (2002) 762.
[34] S. Decker, I. Lagadic, K.J. Klabunde, Chem. Mater. 10 (1998) 674.
[35] E. Lucas, S. Decker, A. Khaleel, A. Seitz, S. Fultz, A. Ponce, W. Li, C. Carnes, K. Klabunde, Chem. Eur. J. 7 (2001) 2505.
[36] K.J. Klabunde, J. Stark, O. Koper, C. Mohs, D.G. Park, S. Decker, Y. Jiang, I. Lagadic, D. Zhang, J. Phys. Chem. 100 (1996) 12142.
[37] W.S. Epling, L.E. Campbell, A. Yezerets, N.W. Currier, J.E. Parks II, Catal. Rev. 46 (2004) 163.
[38] Y. Sakamoto, K. Okumura, Y. Kizaki, S. Matsunaga, N. Takahashi, H. Shinjoh, J. Catal. 238 (2006) 361.
[39] G. Centi, G.E. Arena, S. Perathoner, J. Catal. 216 (2003) 443.
[40] S. Hodjati, P. Bernhardt, C. Petit, V. Pitchon, A. Kiennemann, Appl. Catal. B Environ. 19 (1998) 221.
[41] Z. Liu, J.A. Anderson, J. Catal. 228 (2004) 243.
[42] A.F. Lee, K. Wilson, R.M. Lambert, C.P. Hubbard, R.G. Hurley, R.W. McCabe, H.S. Gandhi, J. Catal. 184 (1999) 491.
[43] X. Wei, X. Liu, M. Deeba, Appl. Catal. B Environ. 58 (2005) 41.
[44] F. Rohr, U. Göbel, P. Kattwinkel, T. Kreuzer, W. Müller, S. Philipp, P. Gélin, Appl. Catal. B Environ. 70 (2007) 189.
[45] F. Rohr, S.D. Peter, E. Lox, M. Kögel, A. Sassi, L. Juste, C. Rigaudeau, G. Belot, P. Gélin, M. Primet, Appl. Catal. B Environ. 56 (2005) 201.
[46] S. Poulston, R.R. Rajaram, Catal. Today 81 (2003) 603.
[47] FindIT Program for the Inorganic Crystal Structure Database.
[48] L. Olsson, E. Fridell, J. Catal. 210 (2002) 340.
[49] X. Liu, O. Korotkikh, R. Farrauto, Appl. Catal. A 226 (2002) 293.
[50] Y. Sakamoto, K. Higuchi, N. Takahashi, K. Yokota, H. Doi, M. Sugiura, Appl. Catal. B Environ. 23 (1999) 159.
[51] H. Mahzoul, J.F. Brilhac, P. Gilot, Appl. Catal. B Environ. 20 (1999) 47.
[52] N.W. Cant, I.O.Y. Liu, M.J. Patterson, J. Catal. 243 (2006) 309.
[53] D.H. Kim, J. Szanyi, J.H. Kwak, T. Szailer, J. Hanson, C.M. Wang, C.H.F. Peden, J. Phys. Chem. B 110 (2006) 10441.